Journal of Applied Mathematics and Physics, 2025, 13(7), 2542-2556
https://www.scirp.org/journal/jamp
ISSN Online: 2327-4379
ISSN Print: 2327-4352

Waterborne Sound Transmission Loss in Finite Double-Plate Sandwich Structures with Poroelastic Cores

Chao Shen[1,2,3], Feng Zeng[4], Qianfeng Wang[5], Ying Hu[3*]

[1]School of Automation Science and Engineering, South China University of Technology, Guangzhou, China
[2]School of Chemical Engineering and Energy Technology, Dongguan University of Technology, Dongguan, China
[3]Department of Mechanical Engineering, The University of Hong Kong, Hong Kong, China
[4]School of Automation and Electrical Engineering, Chengdu Technological University, Chengdu, China
[5]Aerospace Nanhu Electronic Information Technology Co., Ltd., Jingzhou, China
Email: *huying1226@connect.hku.hk

How to cite this paper: Shen, C., Zeng, F., Wang, Q.F. and Hu, Y. (2025) Waterborne Sound Transmission Loss in Finite Double-Plate Sandwich Structures with Poroelastic Cores. *Journal of Applied Mathematics and Physics*, **13**, 2542-2556.
https://doi.org/10.4236/jamp.2025.137143

Received: June 23, 2025
Accepted: July 28, 2025
Published: July 31, 2025

Abstract

This research investigates the sound transmission loss (STL) characteristics of finite double-plate sandwich structures featuring poroelastic cores and air gaps under external water flow conditions. A theoretical framework, based on Biot's theory and modal decomposition, is developed to analyze fluid-structure interactions, convective flow effects, and various boundary conditions. The study highlights the influence of air gap resonances, the added-mass effect from hydrodynamic loading, and asymmetric plate thickness distributions on STL performance. Results indicate that optimized plate asymmetry enhances STL by leveraging mass-stiffness imbalances, while the directional dependence of incident acoustic waves significantly affects transmission outcomes. These insights offer practical design strategies for developing lightweight, broadband underwater acoustic insulation systems tailored for dynamic marine environments.

Keywords

Sound Transmission Loss, Air Gap Resonances, Fluid-Structure Interaction, Underwater Acoustics, Poroelastic Material

1. Introduction

Effective sound insulation in underwater environments and high-speed transport vehicles must balance broadband noise attenuation with adaptability to complex flow and boundary conditions [1]-[4]. For example, submarine hulls require high sound transmission loss (STL) to ensure stealth, while underwater pipelines

demand noise reduction to safeguard marine ecosystems [5]. Similarly, lightweight acoustic structures in marine vessels enhance passenger comfort by minimizing interior noise.

In air, the significant impedance mismatch between solids (e.g., metals) and air facilitates effective sound reflection, even with thin structures. However, underwater, this impedance contrast is substantially reduced, typically to a ratio of around 10 [6]. For instance, a 4 mm-thick aluminum plate ($Z_{\mathrm{Al}} = 1.73\times10^{7}\ \mathrm{N\cdot s/m^{3}}$) reflects approximately 71% of acoustic energy at 100~Hz in water, compared to over 99.99% in air, due to the smaller impedance difference between air ($Z_{\mathrm{air}} = 412\ \mathrm{N\cdot s/m^{3}}$) and water ($Z_{\mathrm{water}} = 1.48\times10^{6}\ \mathrm{N\cdot s/m^{3}}$). This reduced contrast poses significant challenges for acoustic performance in marine applications [7] [8].

Prior research on convective flow effects in airborne applications has provided valuable insights. Koval [9] identified STL degradation in curved plates due to flow, while Tang *et al.* [10] [11] and Zhou *et al.* [12] extended these findings to sandwich and poroelastic systems. Liu *et al.* [13] [14] developed flow-acoustic coupling models for infinite structures, demonstrating STL improvements through shear stress and resonance suppression. However, the impact of external water flows on finite double-plate systems, particularly under varied boundary conditions, remains largely unexplored. Currently, no comprehensive framework addresses the interaction between finite sandwich structures and external water flows, accounting for factors such as plate thickness distribution with constant total mass, varying poroelastic core heights, and diverse boundary conditions. This gap limits the development of effective underwater sound insulation systems and high-performance panels for submerged or water-exposed environments [15].

This study introduces a validated theoretical model for waterborne sound insulation in finite double-plate sandwich structures with poroelastic cores and air gaps. Grounded in Biot's theory and modal decomposition [16], the model integrates convective flow dynamics and fluid-structure interactions. It systematically evaluates the effects of boundary constraints, resonance phenomena, and hydrostatic pressure on STL. The research offers three key contributions: 1) it demonstrates how varying plate thickness distributions, while maintaining constant total mass, induces an added-mass effect that significantly alters acoustic behavior; 2) it incorporates external water flow dynamics into STL modeling for poroelastic sandwich systems; and 3) it analyzes STL performance across four distinct boundary conditions, providing insights into optimizing acoustic performance in submerged settings. These findings pave the way for designing advanced underwater sound insulation systems and high-performance acoustic barriers for flow-exposed structures.

2. Vibro-Acoustic Theoretical Modeling

Figure 1 shows the geometry and notation for the sound transmission loss problem of a double-plate sandwich with a poroelastic core, immersed in water on the

upper side in **Figure 1(a)** and immersed in water on the bottom side in **Figure 1(b)**. As shown in **Figure 1(a)**, a plane acoustic wave of unit amplitude is incident from the upper water domain (semi-infinite, density ρ_i, sound speed c_i) onto the first aluminium plate (thickness t_1), then propagates through an air gap of height H_{g1}, the poroelastic layer of thickness H_p, a second air gap of height H_{g2}, and finally through the second aluminium plate (thickness t_2) into the lower air domain (semi-infinite, density ρ_t, sound speed c_t). The description about the layering of materials is shown in **Table 1**.

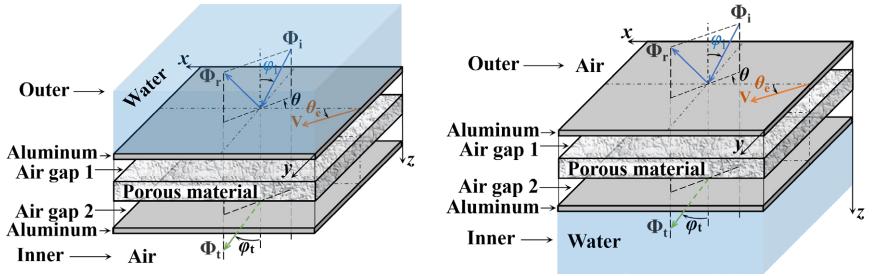

(a) (b)

Figure 1. Schematic diagram of sound transmission through the double-plate structure with poroelastic core: (a) Upper side: water, (b) Bottom side: water.

We adopt a Cartesian (x, y, z) system with the z-axis normal to the plates. The plates themselves extend in the x-y plane over a rectangular area of size $a \times b$; each of their four edges may be subjected to arbitrary boundary conditions (simply supported, clamped, free, etc.). The incident wave makes an elevation angle φ_i with respect to the z-axis (*i.e.* the angle between its propagation direction and the x-y plane normal) and an azimuth angle θ in the x-y plane (measured from the x-axis). By analogy with Snell's law, the same pair of angles (φ_i, θ) describes the direction of each plane-wave component in all layers if there is no mean flow to break the in-plane wavevector continuity.

Table 1. Layering of materials in **Figure 1(a)**.

Layer	Material	Properties/Thickness
1	Water (incident field)	(ρ_i, c_i)
2	Aluminum plate 1	Thickness t_1
3	Air gap 1	Height H_{g1}
4	Poroelastic core	Thickness H_p
5	Air gap 2	Height H_{g2}
6	Aluminum plate 2	Thickness t_2
7	Air (transmission field)	(ρ_t, c_t)

All fluid layers (water domains and air gaps) are assumed quiescent for default

unless otherwise noted, so only acoustic pressure continuity and normal-velocity continuity are enforced at each interface. The poroelastic layer is modeled in full three-dimensional Biot theory, and the two plates are treated as thin, linearly elastic shells. The goal of the theoretical formulation that follows is to compute the complex transmission coefficient through this six-layer stack and hence the STL as a function of frequency, incidence angles (φ_i, θ), plate and layer geometry ($t_1, t_2, H_{g1}, H_p, H_{g2}, a, b$), and material properties.

2.1. Velocity Potential and Wavenumber

As depicted in **Figure 1(a)**, the acoustic field in the upper water region (incident field) comprises an incoming wave and its reflection resulting from interaction with the first aluminum plate. Due to the presence of a uniform external flow in this region, the acoustic velocity potential is expressed in harmonic form as:

$$\Phi_i = \mathrm{e}^{\mathrm{j}\omega t - \mathrm{j}\left(k_{ix}x + k_{iy}y + k_{iz}z\right)} + R\mathrm{e}^{\mathrm{j}\omega t - \mathrm{j}\left(k_{ix}x + k_{iy}y - k_{iz}z\right)}, \tag{1}$$

where the incident wave has a unit amplitude, R represents the complex reflection coefficient, ω denotes the angular frequency, and $\mathrm{j} = \sqrt{-1}$. The Cartesian components of the incident wavenumber are defined as:

$$k_{ix} = k_i \sin\varphi_i \cos\theta, \quad k_{iy} = k_i \sin\varphi_i \sin\theta, \quad k_{iz} = \sqrt{k_i^2 - \left(k_{ix}^2 + k_{iy}^2\right)}.$$

Within the two stationary air gaps (Air gap 1 and Air gap 2) located between the plates and the poroelastic core, the acoustic field consists of forward- and backward-propagating waves. In the absence of flow, the velocity potential in these air gaps adheres to the standard Helmholtz wave equation:

$$\frac{\partial^2 \Phi_{\hat{g}}}{\partial t^2} = c_{\hat{g}}^2 \nabla^2 \Phi_{\hat{g}}, \tag{2}$$

where $\hat{g} \in \{g_1, g_2\}$ indicates either air gap, and $c_{\hat{g}}$ is the speed of sound in the respective gap. The harmonic form of the acoustic velocity potential in each air gap is given by:

$$\Phi_{\hat{g}} = \Phi_{\hat{gi}} + \Phi_{\hat{gr}} = I_{\hat{g}} \mathrm{e}^{\mathrm{j}\omega t - \mathrm{j}\left(k_{\hat{g}x}x + k_{\hat{g}y}y + k_{\hat{g}z}z\right)} + R_{\hat{g}} \mathrm{e}^{\mathrm{j}\omega t - \mathrm{j}\left(k_{\hat{g}x}x + k_{\hat{g}y}y - k_{\hat{g}z}z\right)}, \tag{3}$$

where $I_{\hat{g}}$ and $R_{\hat{g}}$ represent the amplitudes of the incident and reflected wave components in air gap $\hat{g}$.

On the transmission side, the semi-infinite lower fluid domain is anechoically terminated, resulting in a single transmitted acoustic wave. Without external flow in this region, the velocity potential of the transmitted wave is expressed as:

$$\Phi_t = T\mathrm{e}^{\mathrm{j}\omega t - \mathrm{j}\left(k_{tx}x + k_{ty}y + k_{tz}z\right)}, \tag{4}$$

where T is the complex amplitude of the transmitted wave, and the wavenumber k_t in the stationary transmission medium is given by $k_t = \omega / c_t$.

2.2. Boundary Conditions

As illustrated in **Figure 1(a)**, the poroelastic core is positioned between two air

gaps, which in turn are bounded by the incident and transmitting plates. This structure introduces two distinct types of interfaces: 1) the plate-air gap interface and 2) the air gap-poroelastic interface. The governing boundary conditions at these interfaces are derived based on fluid-structure and fluid-poroelastic coupling principles [12], and they can be broadly categorized into two groups: (a) continuity of acoustic velocity and structural displacement, and (b) dynamic equilibrium between acoustic pressure forces and structural response.

2.2.1. Incident Plate Boundary Conditions

At the mid-surface of the incident plate, three boundary conditions must be satisfied to account for the interaction with the incident acoustic field (which includes mean flow) and the adjacent stationary air gap. These are:

$$\text{(i)}\, v_{\mathrm{i}z} = \frac{\mathrm{D}w_{t1}}{\mathrm{D}t}, \quad \text{(ii)}\, v_{\mathrm{g}1z} = \frac{\partial w_{t1}}{\partial t}, \quad \text{(iii)}\, p_{\mathrm{i}} - p_{\mathrm{g}1} = w_{t1}\left[B_{\mathrm{l}}(k_x^2 + k_y^2)^2 - \omega^2 m_{s1}\right]. \tag{5}$$

Here, $v_{\mathrm{i}z}$ and p_{i} represent the normal acoustic particle velocity and acoustic pressure at the surface exposed to the incident field, while $v_{\mathrm{g}1z}$ and $p_{\mathrm{g}1}$ denote their equivalents in the adjacent quiescent air gap. The symbol w_{t1} indicates the transverse displacement of the plate. The first two conditions ensure the continuity of normal velocity and displacement across the plate interface, while the third condition describes the transverse dynamics of the plate as dictated by the Euler-Bernoulli beam equation, characterized by bending stiffness B_{l} and surface mass density m_{s1}.

2.2.2. Poroelastic Layer Interface Boundary Conditions

At each interface between the poroelastic material and its surrounding air gaps (both assumed to be quiescent), four boundary conditions must be enforced:

$$\begin{aligned} &\text{(i)} - \beta p_{\hat{\mathrm{g}}} = s, \quad \text{(ii)} - (1-\beta) p_{\hat{\mathrm{g}}} = \sigma_z, \\ &\text{(iii)}\, v_{\hat{\mathrm{g}}z} = (1-\beta)\frac{\partial u_z}{\partial t} + \beta\frac{\partial U_z}{\partial t}, \quad \text{(iv)}\, \tau_{xz} = \tau_{yz} = 0, \end{aligned} \tag{6}$$

where $p_{\hat{\mathrm{g}}}$ and $v_{\hat{\mathrm{g}}z}$ are the acoustic pressure and normal particle velocity at the air gap-poroelastic interface, which are expressed using the velocity potential $\Phi_{\hat{\mathrm{g}}}$ for the stationary gap medium:

$$p_{\hat{\mathrm{g}}} = \rho_{\hat{\mathrm{g}}}\frac{\partial \Phi_{\hat{\mathrm{g}}}}{\partial t} = \mathrm{j}\omega\rho_{\hat{\mathrm{g}}}\Phi_{\hat{\mathrm{g}}}, \quad v_{\hat{\mathrm{g}}z} = \mathrm{j}k_{\hat{\mathrm{g}}z}\Phi_{\hat{\mathrm{g}}}. \tag{7}$$

The coefficients β and $1-\beta$ are used to distribute the pressure contribution between the fluid and solid phases of the poroelastic medium, while s and σ_z represent the fluid pressure and normal stress in the solid skeleton. The third condition in Equation (6). ensures conservation of the normal velocity at the interface. Finally, the shear stresses τ_{xz} and τ_{yz} are set to zero based on the assumption of inviscid flow in the stationary air gaps.

2.2.3. Transmitting Plate Boundary Conditions

Similarly, the following three boundary conditions must be fulfilled at the mid-

surface of the transmitting plate:

$$(\mathrm{i})\, v_{g2z} = \frac{\partial w_{t2}}{\partial t}, \quad (\mathrm{ii})\, v_{tz} = \frac{\partial w_{t2}}{\partial t}, \quad (\mathrm{iii})\, p_{g2} - p_t = w_{t2}\left[B_2(k_x^2 + k_y^2)^2 - \omega^2 m_{s2}\right]. \quad (8)$$

Here, p_t and v_{tz}, associated with the transmitted field, are defined via the potential function Φ_t as:

$$p_t = \rho_t \frac{\partial \Phi_t}{\partial t} = \mathrm{j}\omega\rho_t\Phi_t, \quad v_{tz} = \mathrm{j}k_{tz}\Phi_t. \quad (9)$$

In these expressions, w_{t2} is the transverse displacement of the transmitting plate, with bending stiffness B_2 and mass per unit area m_{s2}. As before, the first two conditions maintain velocity and displacement continuity across the plate-air interface, and the third describes the dynamic response of the plate under differential acoustic loading.

2.3. Modal Decomposition

The equations governing the flexural motions of two coupled plates with two air gaps are described as follows [17]-[19]:

$$B_1\nabla^4 w_{t1} + m_{s1}\frac{\partial^2 w_{t1}}{\partial t^2} = p_i - p_{g1}, \quad (10a)$$

$$B_2\nabla^4 w_{t2} + m_{s2}\frac{\partial^2 w_{t2}}{\partial t^2} = p_{g2} - p_t, \quad (10b)$$

where $\nabla^4 = \left(\partial^2/\partial x^2 + \partial^2/\partial y^2\right)^2 = \left(k_x^2 + k_y^2\right)^2$ and $\partial^2/\partial t^2 = -\omega^2$. The terms are defined as follows: $p_{g1} = \rho_{g1}\partial\Phi_{g1}/\partial t$, and $p_{g2} = \rho_{g2}\partial\Phi_{g2z}/\partial t$. The term $B_i\nabla^4 w_{ti}$ represents the classical biharmonic operator for bending, while $m_{si}\partial^2 w_{ti}/\partial t^2$ accounts for the inertial resistance of the plate. The flexural stiffness of the plates can be articulated as

$$B_i = \frac{E_i h_i^3\left(1+\mathrm{j}\eta_i\right)}{12\left(1-\nu_i^2\right)} \quad (i=1,2), \quad (11)$$

where E_i, h_i, η_i, and ν_i denote the Young's modulus, thickness, loss factor, and Poisson's ratio of the ith plate, respectively. This expression for complex flexural rigidity is commonly utilized to incorporate damping effects through the loss factor η_i. The inclusion of the complex term $\left(1+\mathrm{j}\eta_i\right)$ is a standard approach in harmonic analysis to account for losses in a phenomenological manner. Following previous studies [17]-[20], the transverse displacements w_{t1} and w_{t2} can be written as a modal decomposition:

$$w_{t1}(x,y,t) = \sum_{m,n}\phi_{mn}(x,y)\alpha_{1,mn}\mathrm{e}^{\mathrm{j}\omega t}, \quad w_{t2}(x,y,t) = \sum_{m,n}\phi_{mn}(x,y)\alpha_{2,mn}\mathrm{e}^{\mathrm{j}\omega t}, \quad (12)$$

where $\alpha_{1,mn}$ and $\alpha_{2,mn}$ are the modal displacement coefficients of the upper and bottom plates, respectively. **Table 2** provides the details for other types of edge supports.

Given the expressions for the incident and transmitted waves, Φ_i and Φ_t, in Equations (1) and (4), we can now utilize the continuity of normal velocity at

Table 2. Summary of boundary conditions and modal functions for rectangular plates.

Boundary Condition	Description	Modal Function $\phi_{mn}(x,y)$
CCCC	All edges clamped (fully clamped)	$\left(1-\cos\left(\frac{2m\pi x}{a}\right)\right)\left(1-\cos\left(\frac{2n\pi y}{b}\right)\right)$
SSSS	All edges simply supported	$\sin\left(\frac{m\pi x}{a}\right)\sin\left(\frac{n\pi y}{b}\right)$
FFFF	All edges free (free-free plate)	$\cos\left(\frac{(m-1)\pi x}{a}\right)\cos\left(\frac{(n-1)\pi y}{b}\right)$
CCSS	Mixed clamped and simply supported	$\left(1-\cos\left(\frac{2m\pi x}{a}\right)\right)\sin\left(\frac{n\pi y}{b}\right)$

the interfaces of the two plates. Substituting these expressions into the boundary conditions given by Equations 5(i) and 8(ii) allows us to derive the amplitudes of the reflected and transmitted waves, R and T, as:

$$R(x,y)=1-\frac{e^{j(k_x x+k_y y)}}{k_{iz}}\sum_{m,n}\left(\omega\phi_{mn}-j\boldsymbol{V}\cdot\nabla\phi_{mn}\right)\alpha_{1,mn}, \tag{13}$$

$$T(x,y)=\frac{\omega}{k_{tz}}e^{j\left(k_x x+k_y y+k_{tz}\left(L_{g1}+H_p+L_{g2}\right)\right)}\sum_{m,n}\phi_{mn}\alpha_{2,mn}. \tag{14}$$

The detailed expressions of the boundary condition equations in Equations (5)-(8) can be seen in Appendix A. Using the Equations (A.1) and (A.10) one can obtain the expressions of Φ_i and Φ_t: The other Equations (A.2)-(A.9) together lead to a system of 8 equations. Therefore, the complex constants ($C_1, C_2, C_3, C_4, I_{g1}, R_{g1}, I_{g2}$ and R_{g2}) can be determined by a 8×8 matrix equation:

$$\boldsymbol{MC}=\boldsymbol{S} \tag{15}$$

where

$$\boldsymbol{C}=\left[C_1\ C_2\ C_3\ C_4\ I_{g1}\ R_{g1}\ I_{g2}\ R_{g2}\right]^t, \tag{16}$$

$$\boldsymbol{S}=\left[\sum_{m,n}\alpha_{1,mn}\phi_{mn}e^{j(k_x x+k_y y)}\ 0\ 0\ 0\ 0\ 0\ \sum_{m,n}\alpha_{2,mn}\phi_{mn}e^{j(k_x x+k_y y)}\right]^t. \tag{17}$$

2.4. The Galerkin Method

To determine the unknown modal coefficients $\alpha_{1,mn}$, $\alpha_{2,mn}$, and $\alpha_{3,mn}$, the principle of virtual work is employed. The virtual work δ_i resulting from a force acting on a particle through a virtual displacement (an infinitesimal change in the particle's position consistent with the system's constraints) is given by:

$$\delta_i=\delta\alpha_{i,mn}\phi_{mn}(x,y)\ (i=1,2). \tag{18}$$

The sum of these virtual work contributions over the entire system must equal zero. Applying the Galerkin method to the equations of motion for the plate,

Equations (10a) and (10b), involves integrating weighted functions over the domain of the double-plate configuration. The weak form of the principle of virtual work can be expressed as:

$$\int_0^b \int_0^a \left(B_1 \nabla^4 w_{t1} + m_{s1} \frac{\partial^2 w_{t1}}{\partial^2 t} - p_{\mathrm{i}} + p_{\mathrm{g1}} \right) \delta_1 \mathrm{d}x\mathrm{d}y = 0, \tag{19}$$

$$\int_0^b \int_0^a \left(B_2 \nabla^4 w_{t2} + m_{s2} \frac{\partial^2 w_{t2}}{\partial^2 t} - p_{\mathrm{g2}} + p_{\mathrm{t}} \right) \delta_2 \mathrm{d}x\mathrm{d}y = 0. \tag{20}$$

The variables $\Phi_{\mathrm{i}}, \Phi_{\mathrm{g1}}, \Phi_{\mathrm{g2}}, \Phi_t$ in $p_{\mathrm{i}}, p_{\mathrm{g1}}, p_{\mathrm{g2}}$ and p_{t}, and w_{t1}, w_{t2} have been expressed in terms of $\alpha_{1,mn}$ and $\alpha_{2,mn}$ using the solution of the unknown vector $\boldsymbol{C}$.

2.5. Sound Transmission Loss

Sound intensity in the incident or transmitted field is given by:

$$I = \frac{1}{2} \mathrm{Re}\left(p v^* \right), \tag{21}$$

where v^* is the complex conjugate of acoustic velocity v, and $\mathrm{Re}(\cdot)$ denotes the real part. The incident and transmitted acoustic power over plate surface area S are:

$$\Pi_{\mathrm{i}} = \frac{1}{2} \mathrm{Re}\left[\int_S p_{\mathrm{i}} v_{\mathrm{iz}}^* \mathrm{d}S \right], \quad \Pi_{\mathrm{t}} = \frac{1}{2} \mathrm{Re}\left[\int_S p_{\mathrm{t}} v_{\mathrm{tz}}^* \mathrm{d}S \right], \tag{22}$$

where $p_{\mathrm{i}}, p_{\mathrm{t}}, v_{\mathrm{iz}}$, and v_{tz} represent pressure and velocity fields in the incident and transmitted domains. The power transmission coefficient for a single incident wave is:

$$\tau\left(\varphi_{\mathrm{i}}, \theta\right) = \frac{\Pi_{\mathrm{t}}}{\Pi_{\mathrm{i}}}. \tag{23}$$

Sound transmission loss (STL), expressed in decibels, is:

$$\mathrm{STL} = 10 \log\left(\frac{1}{\tau} \right). \tag{24}$$

This metric evaluates acoustic system performance, with details in prior studies [12] [21].

3. Results and Discussion

3.1. Parameters of the Systems

To study external flow and poroelastic core effects on STL in a double-plate sandwich structure, material parameters from [12] [21]-[23] are used. Both aluminum face plates have identical properties, with thicknesses $t_1 = t_2 = 2$ mm. The poroelastic layer, made of polyurethane foam, follows parameters in [21] [23]. The incident and transmission media are water at standard room temperature properties. Air gaps have heights $H_{\mathrm{g1}} = H_{\mathrm{g2}} = 0.01$ m, with no internal flow, yielding a total system height $H_{\mathrm{t}} = 0.041$ m. Unless specified, the incident wave's azimuthal

angle is $\theta = 0^\circ$, and external flow aligns with the x-axis ($\theta_e = 0^\circ$).

3.2. Impact of Boundary Conditions and Plate Dimensions on STL

The influence of boundary conditions and plate dimensions on the STL of rectangular plates subjected to normal sound incidence in the absence of external flow ($M = 0$) is depicted in **Figure 2**. Four distinct boundary conditions are examined: (a) fully clamped (CCCC), (b) simply supported (SSSS), (c) free-free (FFFF), and (d) mixed clamped and simply supported (CCSS). The STL is plotted against frequency for four different square plate dimensions: $a = b = 0.125$ m, $a = b = 0.25$ m, $a = b = 0.5$ m, and $a = b = 1$ m.

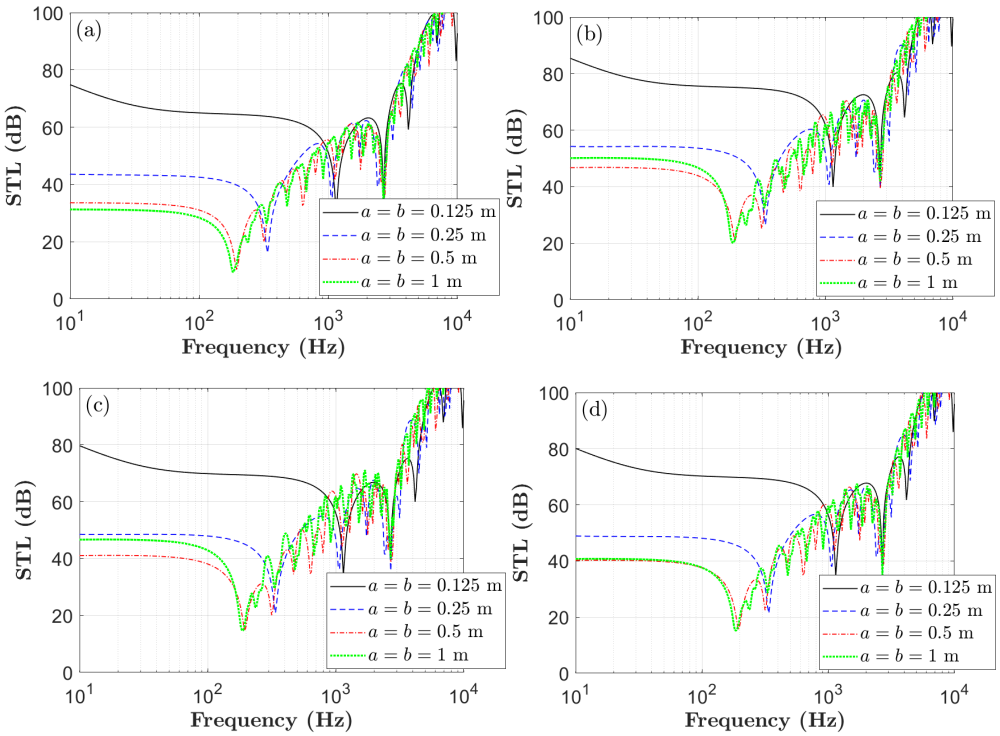

Figure 2. Impact of boundary conditions: (a) CCCC, (b) SSSS, (c) FFFF, (d) CCSS on the STL without external flow ($M = 0$) at an incidence angle $\varphi_i = 0^\circ$.

The effect of boundary conditions on STL varies with frequency. The CCCC condition shows a significant STL dip at the fundamental resonance due to reduced damping from rigid edge clamping, while the SSSS condition yields the highest STL below this resonance. Smaller plates ($a = b = 0.125$ m) exhibit higher STL at frequencies above 1000 Hz, outperforming larger plates ($a = b = 1$ m), which show lower STL in this range. This is attributed to smaller plates having higher natural frequencies, leading to more pronounced resonant STL dips at higher frequencies.

3.3. Effect of Air Gap Height and External Water Flow

The impact of air gap height (H_g, defined as the sum of $H_{g1} + H_{g2}$ in the

absence of a poroelastic layer) and external grazing flow (V) on sound transmission loss (STL) is analyzed for two angles of sound incidence: normal incidence ($\varphi_i = 0^\circ$) and oblique incidence ($\varphi_i = 45^\circ$). **Figure 3(a)** presents the STL results for normal incidence. When there is no flow ($V = 0$ m/s), increasing the air gap height from 0.01 m to 0.04 m causes the characteristic peaks and dips in the STL spectrum to shift to lower frequencies. For example, the first significant dip in STL moves from around 280 Hz for $H_g = 0.01$ m to below 150 Hz for $H_g = 0.04$ m. This behavior is typical of cavity-backed acoustic systems, where the air gap functions as a quarter-wavelength resonator at its harmonic frequencies. When comparing the no-flow condition ($V = 0$ m/s) to the case with grazing flow ($V = 17$ m/s) for each gap height, the presence of flow leads to improved STL at very low frequencies (e.g., below 70 Hz). However, the dominant factor influencing the shift in resonance frequencies continues to be the height of the air gap. At frequencies higher than the extra low frequency, the impact of the grazing water flow at this velocity is quite limited.

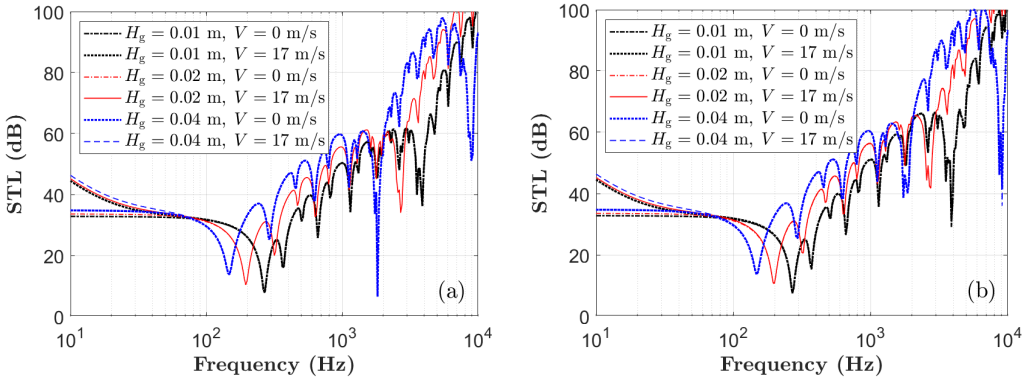

Figure 3. Effect of air gap heights with/without external water flow at incidence angle: (a) $\varphi_i = 0^\circ$, (b) $\varphi_i = 45^\circ$.

By comparing **Figure 3(a)** and **Figure 3(b)**, it becomes clear that raising the air gap height effectively adjusts the STL performance to lower frequencies by shifting the plate-air-plate resonances. The angle of incidence only slightly affects the overall shape and magnitude of the STL spectrum. Ultimately, the air gap height is the main factor influencing the position of the resonance frequencies.

3.4. Influence of Plate Thickness Distribution and Added-Mass Effect

Figure 4(a) shows the STL behavior of a double-plate system with fully clamped (CCCC) boundary conditions, without a porous core. The structure consists of two aluminum plates with a fixed total thickness of 4 mm, varying between the upper (t_1) and lower (t_2) plates. The upper medium is water, the inter-plate cavity and lower medium are air, with acoustic excitation at normal incidence ($\varphi_i = 0^\circ$), no mean flow ($M = 0$), and an air gap height of $H_g = 0.02$ m.

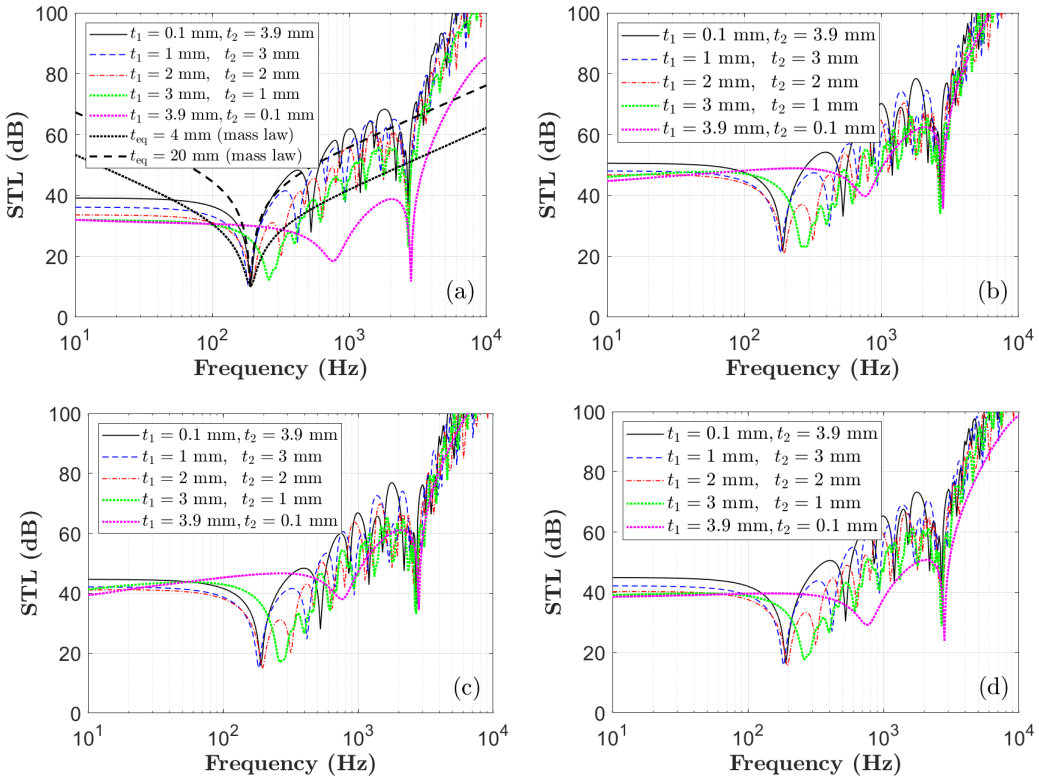

Figure 4. Impact of various boundary conditions on the STL under conditions of no external water flow ($M = 0$) at normal incidence ($\varphi_i = 0^\circ$), where the upper domain is water, and both the middle gap and bottom domain are air: (a) CCCC, (b) SSSS, (c) FFFF, and (d) CCSS. The air gap height is 0.02 m, and no porous layer is included in the gap. The plate dimensions are $a = b = 0.5$ m , with the thicknesses of the upper and lower plates represented by t_1 and t_2 , and the unchanged total height of both plates combined is 4 mm.

Added-Mass Effect

STL generally follows the mass-law, increasing by 6 dB per doubling of surface mass density. However, fluid-structure interaction with water induces an added-mass effect, increasing the plates' apparent mass and inertial impedance. This enhances STL in the mid-frequency range, exceeding mass-law predictions. For example, the configuration with $t_1 = 0.1$ mm and $t_2 = 3.9$ mm outperforms the $t_{eq} = 4$ mm mass-law prediction below 500 Hz, lowering resonance frequencies by 50 Hz and boosting STL by 5 - 10 dB in the 200 - 500 Hz range, compared to an air-only scenario with reduced inertial resistance.

Air Gap Resonances

In the 200 Hz - 10 kHz band, STL surpasses mass-law predictions due to the air gap's acoustic behavior, which creates impedance mismatch and supports internal reflections and standing waves, enhancing modal suppression. STL is sensitive to plate thickness distribution:

- The asymmetric case ($t_1 = 0.1$ mm , $t_2 = 3.9$ mm) matches the STL of a $t_{eq} = 20$ mm monolithic plate, driven by mass-stiffness asymmetry and optimal impedance.

- The case with $t_1 = 3$ mm and $t_2 = 1$ mm resembles the uniform $t_{eq} = 4$ mm case, with less STL enhancement.

These results highlight that STL depends not only on total mass but also on structural impedance distribution and cavity dynamics.

4. Conclusions

This study provides a detailed examination of waterborne sound transmission through finite double-plate sandwich structures with poroelastic cores and air gaps, incorporating the effects of external water flow. Utilizing a robust theoretical model grounded in Biot's theory and modal decomposition, the research uncovers critical mechanisms governing STL performance. Key findings include:

1) Asymmetric plate thickness distributions, maintaining constant total mass, significantly enhance STL through mass-stiffness asymmetry, with configurations like a thin upper plate ($t_1 = 0.1$ mm) and thick lower plate ($t_2 = 3.9$ mm) achieving performance comparable to much thicker monolithic plates.

2) The added mass effect from hydrodynamic loading increases effective plate mass, reducing resonance frequencies and boosting STL by 5 - 10 dB in the 200 - 500 Hz range.

3) Air gap heights critically influence resonance frequencies, shifting STL peaks and dips to lower frequencies as gap height increases.

These findings emphasize the importance of integrating fluid-structure interactions and geometric optimization in designing efficient underwater sound insulation systems. Future work could explore graded poroelastic materials and advanced optimization techniques to further improve STL while minimizing structural weight, advancing applications in marine engineering and submerged environments.

Acknowledgements

The authors acknowledge the support from National Natural Science Foundation of China (Grant No. 12202102), Guangdong Provincial University Innovation Team Project, No. 2023KCXTD038, Guangdong Provincial Key Laboratory of Distributed Energy Systems and the Center for Computational Science and Engineering at the Southern University of Science and Technology.

Conflicts of Interest

The authors declare no conflicts of interest regarding the publication of this paper.

References

[1] H. Yang, H., Xiao, Y., Zhao, H., Zhong, J. and Wen, J. (2019) On Wave Propagation and Attenuation Properties of Underwater Acoustic Screens Consisting of Periodically Perforated Rubber Layers with Metal Plates. *Journal of Sound and Vibration*, **444**, 21-34. https://doi.org/10.1016/j.jsv.2018.12.031

[2] Sharma, G.S., Skvortsov, A., MacGillivray, I. and Kessissoglou, N. (2017) Sound

Transmission through a Periodically Voided Soft Elastic Medium Submerged in Water. *Wave Motion*, **70**, 101-112. https://doi.org/10.1016/j.wavemoti.2016.10.006

[3] Tu, H., Wang, Y., Yang, C., Liu, W. and Wang, X. (2023) A Chebyshev-Tau Spectral Method for Coupled Modes of Underwater Sound Propagation in Range-Dependent Ocean Environments. *Physics of Fluids*, **35**, Article ID: 037113. https://doi.org/10.1063/5.0138012

[4] Li, K., Zhou, Z., Huang, Z., Lin, Y., Chen, M., Yang, P., *et al.* (2023) Underwater Sound Absorption Characteristic of the Rubber Core Sandwich Structure with Funnel-Shaped Cavities Reinforced by Carbon Fiber Columns. *Applied Acoustics*, **208**, 109375. https://doi.org/10.1016/j.apacoust.2023.109375

[5] Zhang, D., Zhang, Y., Zhao, B., Ma, Y. and Si, K. (2024) Exploring Subsea Dynamics: A Comprehensive Review of Underwater Pipelines and Cables. *Physics of Fluids*, **36**, Article ID: 101304. https://doi.org/10.1063/5.0231898

[6] Qiang, W., Li, N., Kang, Y., Huang, X., Li, C., Liu, W., *et al.* (2022) Experimental Study on the Transmission Characteristics of Near-Field Detonation Noise into Water. *Physics of Fluids*, **34**, Article ID: 113325. https://doi.org/10.1063/5.0119227

[7] Mallik, W., Jaiman, R. and Jelovica, J. (2024) Deep Neural Network for Learning Wave Scattering and Interference of Underwater Acoustics. *Physics of Fluids*, **36**, Article ID: 017137. https://doi.org/10.1063/5.0188250

[8] Ma, X., Wang, Y., Zhou, X., Xu, G. and Gao, D. (2024) A Chebyshev Tau Matrix Method to Directly Solve Two-Dimensional Ocean Acoustic Propagation in Undulating Seabed Environment. *Physics of Fluids*, **36**, Article ID: 096601. https://doi.org/10.1063/5.0219188

[9] Koval, L.R. (1976) Effect of Air Flow, Panel Curvature, and Internal Pressurization on Field-Incidence Transmission Loss. *The Journal of the Acoustical Society of America*, **59**, 1379-1385. https://doi.org/10.1121/1.381024

[10] Tang, Y., Robinson, J. and Silcox, R. (1996) Sound Transmission through a Cylindrical Sandwich Shell with Honeycomb Core. 34*th Aerospace Sciences Meeting and Exhibit*, Reno, 15-18 January 1996, 877-886. https://doi.org/10.2514/6.1996-877

[11] Tang, Y.Y., Silcox, R. and Robinson, J.H. (1996) Sound Transmission through Two Concentric Cylindrical Sandwich Shells. *Proceedings of the* 14*th International Modal Analysis Conference, Detroit*, 12-15 February 1996, 1488-1495.

[12] J. Zhou, J., Bhaskar, A. and Zhang, X. (2013) Sound Transmission through a Double-Panel Construction Lined with Poroelastic Material in the Presence of Mean Flow. *Journal of Sound and Vibration*, **332**, 3724-3734. https://doi.org/10.1016/j.jsv.2013.02.020

[13] Liu, Y. and Catalan, J. (2017) External Mean Flow Influence on Sound Transmission through Finite Clamped Double-Wall Sandwich Panels. *Journal of Sound and Vibration*, **405**, 269-286. https://doi.org/10.1016/j.jsv.2017.05.049

[14] Liu, Y. and He, C. (2016) Diffuse Field Sound Transmission through Sandwich Composite Cylindrical Shells with Poroelastic Core and External Mean Flow. *Composite Structures*, **135**, 383-396. https://doi.org/10.1016/j.compstruct.2015.09.025

[15] Tarkashvand, A. and Zafari, H. (2025) Innovative Noise-Cancellation Strategies for Fluid-Immersed Cylindrical Structures Using Viscous Rotational Flow and Porous Functionally Graded Piezoelectric Materials. *Physics of Fluids*, **37**, Article ID: 023123. https://doi.org/10.1063/5.0252154

[16] Shen, C., Zhang, H. and Liu, Y. (2019) Analytical Modelling of Sound Transmission Loss across Finite Clamped Triple-Wall Sandwich Panels in the Presence of External

Mean Flow. *Applied Mathematical Modelling*, **73**, 146-165. https://doi.org/10.1016/j.apm.2019.03.043

[17] Xin, F.X. and Lu, T.J. (2009) Analytical and Experimental Investigation on Transmission Loss of Clamped Double Panels: Implication of Boundary Effects. *The Journal of the Acoustical Society of America*, **125**, 1506-1517. https://doi.org/10.1121/1.3075766

[18] Xin, F.X., Lu, T.J. and Chen, C.Q. (2008) Vibroacoustic Behavior of Clamp Mounted Double-Panel Partition with Enclosure Air Cavity. *The Journal of the Acoustical Society of America*, **124**, 3604-3612. https://doi.org/10.1121/1.3006956

[19] Daudin, C. and Liu, Y. (2016) Vibroacoustic Behaviour of Clamped Double-Wall Panels Lined with Poroelastic Materials. *Proceedings of the* 23*rd International Congress on Sound and Vibrations*, Athenes, 10-14 July 2016, 1-8.

[20] Shen, C., Catalan, J. and Liu, Y. (2018) Effects of External and Air Gap Flows on Sound Transmission through Finite Clamped Double-Panel Sandwich Structures. *Composite Structures*, **203**, 286-299. https://doi.org/10.1016/j.compstruct.2018.06.104

[21] Liu, Y. and Sebastian, A. (2015) Effects of External and Gap Mean Flows on Sound Transmission through a Double-Wall Sandwich Panel. *Journal of Sound and Vibration*, **344**, 399-415. https://doi.org/10.1016/j.jsv.2015.01.040

[22] Bolton, J.S., Shiau, N.-. and Kang, Y.J. (1996) Sound Transmission through Multi-Panel Structures Lined with Elastic Porous Materials. *Journal of Sound and Vibration*, **191**, 317-347. https://doi.org/10.1006/jsvi.1996.0125

[23] Liu, Y. (2015) Sound Transmission through Triple-Panel Structures Lined with Poroelastic Materials. *Journal of Sound and Vibration*, **339**, 376-395. https://doi.org/10.1016/j.jsv.2014.11.014

Appendix A: Expressions of the Boundary Condition Equations

By applying the expressions of all the elements in Equations (5)-(8), one can obtain the following equations:

At $z=0$:

$$(\mathrm{i})\ \mathrm{j}k_{\mathrm{iz}}\left(1-R\right)\mathrm{e}^{-\mathrm{j}\left(k_x x+k_y y\right)}=\sum_{m,n}\alpha_{1,mn}\left[\mathrm{j}\omega\phi_{mn}+\boldsymbol{V}\cdot\nabla\phi_{mn}\right] \tag{A.1}$$

$$(\mathrm{ii})\ \frac{k_{\mathrm{g1}z}}{\omega}\left(-I_{\mathrm{g1}}+R_{\mathrm{g1}}\right)\mathrm{e}^{-\mathrm{j}\left(k_x x+k_y y\right)}=\sum_{m,n}\alpha_{1,mn}\phi_{mn}\ . \tag{A.2}$$

At $z=L_{\mathrm{g1}}$:

$$\begin{aligned}&(\mathrm{i})-\mathrm{j}\omega\beta\rho_{\mathrm{g}}I_{\mathrm{g1}}\mathrm{e}^{-\mathrm{j}k_{\mathrm{g1}z}L_{\mathrm{g1}}}+R_{\mathrm{g1}}\mathrm{e}^{\mathrm{j}k_{\mathrm{g1}z}L_{\mathrm{g1}}}\\&=\left[N_1\left(C_1\mathrm{e}^{-\mathrm{j}k_{\mathrm{i}z}L_{\mathrm{g1}}}+C_2\mathrm{e}^{\mathrm{j}k_{\mathrm{i}z}L_{\mathrm{g1}}}\right)+N_2\left(C_3\mathrm{e}^{-\mathrm{j}k_{\mathrm{II}z}L_{\mathrm{g1}}}+C_4\mathrm{e}^{\mathrm{j}k_{\mathrm{II}z}L_{\mathrm{g1}}}\right)\right]\end{aligned} \tag{A.3}$$

$$\begin{aligned}&(\mathrm{ii})-\mathrm{j}\omega\left(1-\beta\right)\rho_{\mathrm{g}}I_{\mathrm{g1}}\mathrm{e}^{-\mathrm{j}k_{\mathrm{g1}z}L_{\mathrm{g1}}}+R_{\mathrm{g1}}\mathrm{e}^{\mathrm{j}k_{\mathrm{g1}z}L_{\mathrm{g1}}}\\&=\left[L_1\left(C_1\mathrm{e}^{-\mathrm{j}k_{\mathrm{i}z}L_{\mathrm{g1}}}+C_2\mathrm{e}^{\mathrm{j}k_{\mathrm{i}z}L_{\mathrm{g1}}}\right)+L_2\left(C_3\mathrm{e}^{-\mathrm{j}k_{\mathrm{II}z}L_{\mathrm{g1}}}+C_4\mathrm{e}^{\mathrm{j}k_{\mathrm{II}z}L_{\mathrm{g1}}}\right)\right]\end{aligned} \tag{A.4}$$

$$\begin{aligned}&(\mathrm{iii})-k_{\mathrm{g1}z}\left(-I_{\mathrm{g1}}\mathrm{e}^{-\mathrm{j}k_{\mathrm{g1}z}L_{\mathrm{g1}}}+R_{\mathrm{g1}}\mathrm{e}^{\mathrm{j}k_{\mathrm{g1}z}L_{\mathrm{g1}}}\right)\\&=\left[\left(1-\beta\right)\left(C_1M_1\mathrm{e}^{-\mathrm{j}k_{\mathrm{i}z}L_{\mathrm{g1}}}-C_2M_1\mathrm{e}^{\mathrm{j}k_{\mathrm{i}z}L_{\mathrm{g1}}}+C_3M_2\mathrm{e}^{-\mathrm{j}k_{\mathrm{II}z}L_{\mathrm{g1}}}-C_4M_2\mathrm{e}^{\mathrm{j}k_{\mathrm{II}z}L_{\mathrm{g1}}}\right)\right.\\&\left.+\omega\beta\left(b_1C_1M_1\mathrm{e}^{-\mathrm{j}k_{\mathrm{i}z}L_{\mathrm{g1}}}-b_1C_2M_1\mathrm{e}^{\mathrm{j}k_{\mathrm{i}z}L_{\mathrm{g1}}}+b_2C_3M_2\mathrm{e}^{-\mathrm{j}k_{\mathrm{II}z}L_{\mathrm{g1}}}-b_2C_4M_2\mathrm{e}^{\mathrm{j}k_{\mathrm{II}z}L_{\mathrm{g1}}}\right)\right].\end{aligned} \tag{A.5}$$

At $z=L_{g1}+H_p$:

$$\begin{aligned}&(\mathrm{i})-\mathrm{j}\omega\beta\rho_{\mathrm{g}}I_{\mathrm{g2}}\mathrm{e}^{-\mathrm{j}k_{\mathrm{g2}z}\left(L_{\mathrm{g1}}+H_{\mathrm{p}}\right)}+R_{\mathrm{g2}}e^{jk_{g2z}\left(L_{\mathrm{g1}}+H_{\mathrm{p}}\right)}\\&=\left[N_1\left(C_1\mathrm{e}^{-\mathrm{j}k_{\mathrm{i}z}\left(L_{\mathrm{g1}}+H_{\mathrm{p}}\right)}+C_2\mathrm{e}^{\mathrm{j}k_{\mathrm{i}z}\left(L_{\mathrm{g1}}+H_{\mathrm{p}}\right)}\right)+N_2\left(C_3\mathrm{e}^{-\mathrm{j}k_{\mathrm{II}z}\left(L_{\mathrm{g1}}+H_{\mathrm{p}}\right)}+C_4\mathrm{e}^{\mathrm{j}k_{\mathrm{II}z}\left(L_{\mathrm{g1}}+H_{\mathrm{p}}\right)}\right)\right]\end{aligned} \tag{A.6}$$

$$\begin{aligned}&(\mathrm{ii})-\mathrm{j}\omega\left(1-\beta\right)\rho_g\left(I_{\mathrm{g2}}\mathrm{e}^{-\mathrm{j}k_{\mathrm{g2}z}\left(L_{\mathrm{g1}}+H_{\mathrm{p}}\right)}+R_{\mathrm{g2}}\mathrm{e}^{\mathrm{j}k_{\mathrm{g2}z}\left(L_{\mathrm{g1}}+H_{\mathrm{p}}\right)}\right)\\&=\left[L_1\left(C_1\mathrm{e}^{-\mathrm{j}k_{\mathrm{i}z}\left(L_{\mathrm{g1}}+H_{\mathrm{p}}\right)}+C_2\mathrm{e}^{\mathrm{j}k_{\mathrm{i}z}\left(L_{\mathrm{g1}}+H_{\mathrm{p}}\right)}\right)+L_2\left(C_3\mathrm{e}^{-\mathrm{j}k_{\mathrm{II}z}\left(L_{\mathrm{g1}}+H_{\mathrm{p}}\right)}+C_4\mathrm{e}^{\mathrm{j}k_{\mathrm{II}z}\left(L_{\mathrm{g1}}+H_{\mathrm{p}}\right)}\right)\right]\end{aligned} \tag{A.7}$$

$$\begin{aligned}&(\mathrm{iii})-\left(-I_{\mathrm{g2}}\mathrm{e}^{-\mathrm{j}k_{\mathrm{g2}z}\left(L_{\mathrm{g1}}+H_{\mathrm{p}}\right)}+R_{\mathrm{g2}}\mathrm{e}^{jk_{g2z}\left(L_{\mathrm{g1}}+H_{\mathrm{p}}\right)}\right)k_{\mathrm{g}z}\\&=\left[\left(1-\beta\right)\left(C_1M_1\mathrm{e}^{-\mathrm{j}k_{\mathrm{i}z}\left(L_{\mathrm{g1}}+H_{\mathrm{p}}\right)}-C_2M_1\mathrm{e}^{\mathrm{j}k_{\mathrm{i}z}\left(L_{\mathrm{g1}}+H_{\mathrm{p}}\right)}+C_3M_2\mathrm{e}^{-\mathrm{j}k_{\mathrm{II}z}\left(L_{\mathrm{g1}}+H_{\mathrm{p}}\right)}-C_4M_2\mathrm{e}^{\mathrm{j}k_{\mathrm{II}z}\left(L_{\mathrm{g1}}+H_{\mathrm{p}}\right)}\right)\right.\\&\left.+\omega\beta\left(b_1C_1M_1\mathrm{e}^{-\mathrm{j}k_{\mathrm{i}z}\left(L_{\mathrm{g1}}+H_{\mathrm{p}}\right)}-b_1C_2M_1\mathrm{e}^{\mathrm{j}k_{\mathrm{i}z}\left(L_{\mathrm{g1}}+H_{\mathrm{p}}\right)}+b_2C_3M_2\mathrm{e}^{-\mathrm{j}k_{\mathrm{II}z}\left(L_{\mathrm{g1}}+H_{\mathrm{p}}\right)}-b_2C_4M_2\mathrm{e}^{\mathrm{j}k_{\mathrm{II}z}\left(L_{\mathrm{g1}}+H_{\mathrm{p}}\right)}\right)\right].\end{aligned} \tag{A.8}$$

At $z=L_{\mathrm{g1}}+H_{\mathrm{p}}+L_{\mathrm{g2}}$:

$$\begin{aligned}&(\mathrm{i})-\left(-I_{\mathrm{g2}}\mathrm{e}^{-\mathrm{j}k_{\mathrm{g2}z}\left(L_{\mathrm{g1}}+H_{\mathrm{p}}+L_{\mathrm{g2}}\right)}+R_{\mathrm{g2}}\mathrm{e}^{\mathrm{j}k_{\mathrm{g2}z}\left(L_{\mathrm{g1}}+H_{\mathrm{p}}+L_{\mathrm{g2}}\right)}\right)\mathrm{e}^{-\mathrm{j}\left(k_x x+k_y y\right)}k_{\mathrm{g2}z}\\&=\omega\sum_{m,n}\alpha_{2,mn}\phi_{mn}\end{aligned} \tag{A.9}$$

$$(\mathrm{ii})\ k_{\mathrm{t}z}T\mathrm{e}^{-\mathrm{j}\left(k_x x+k_y y+k_{\mathrm{t}z}\left(L_{\mathrm{g1}}+H_{\mathrm{p}}+L_{\mathrm{g2}}\right)\right)}=\omega\sum_{m,n}\alpha_{2,mn}\phi_{mn}\ . \tag{A.10}$$